JOURNAL OF SYNCHROTRON RADIATION

ISSN 1600-5775

Revealing phase boundaries by weighted parametric structural refinement

Frederick Marlton,[a,b]* Stefano Checchia[c,d] and John Daniels[b]

[a]Department of Chemistry and iNANO, Aarhus University, Langelandsgade, Aarhus 8000, Denmark, [b]School of Materials Science and Engineering, UNSW, Sydney, NSW 2052, Australia, [c]European Synchrotron Radiation Facility, 38000 Grenoble, France, and [d]MAX IV Laboratory, Lund University, 22100 Lund, Sweden. *Correspondence e-mail: fredm@inano.au.dk

Received 15 February 2019
Accepted 2 June 2019

Edited by V. Favre-Nicolin, CEA and Université Joseph Fourier, France

Keywords: parametrics; powder diffraction; ferroelectrics; Rietveld refinement.

Supporting information: this article has supporting information at journals.iucr.org/s

Parametric Rietveld refinement from powder diffraction data has been utilized in a variety of situations to understand structural phase transitions of materials *in situ*. However, when analysing data from lower-resolution two-dimensional detectors or from samples with overlapping Bragg peaks, such transitions become difficult to observe. In this study, a weighted parametric method is demonstrated whereby the scale factor is restrained via an inverse tan function, making the phase boundary composition a refinable parameter. This is demonstrated using compositionally graded samples within the lead-free piezoelectric $(BiFeO_3)_x(Bi_{0.5}K_{0.5}TiO_3)_y(Bi_{0.5}Na_{0.5}TiO_3)_{1-x-y}$ and $(Bi_{0.5}Na_{0.5}TiO_3)_x(BaTiO_3)_{1-x}$ systems. This has proven to be an effective method for diffraction experiments with relatively low resolution, weak peak splitting or compositionally complex multiphase samples.

1. Introduction

Phase analysis of a powder diffraction pattern plays an important role in materials science. Being able to quantify the phases present in a sample is necessary in the development of all materials, including electroceramics (Daniels, 2008), cements (Scarlett *et al.*, 2001), metallic alloys (Clancy *et al.*, 2017), minerals and pharmaceuticals (Scarlett *et al.*, 2002).

Using structural analysis, the boundaries in the phase diagram of a solid solution can be determined by measuring the powder diffraction patterns of several samples prepared with different compositions. Here, multipattern, multiphase Rietveld refinements are carried out, whereby the scale factors of each phase relate to their respective weight or molar fractions. The values of some refinable parameters will be independent of composition (*e.g.* instrumental line-profile, absorption). However, structural parameters will be correlated between successive refinements and thus dependent on their compositional coordinates (Daniels *et al.*, 2010). Therefore, instead of fitting n parameters in m-independent Rietveld refinements, one can obtain the dependence of the key parameters on composition through a parametric multipattern refinement (Olsen *et al.*, 2017). This reduces the number of free variables, their correlation and, in turn, the standard uncertainties of their values. In practice, a parametric Rietveld refinement involves determining equations for structural parameters (*e.g.* lattice parameters, atomic positions, occupancies, scale factor) as a function of a variable (*e.g.* composition, temperature or pressure) in order to restrain the Rietveld refinement to fit a three-dimensional space of 2θ, intensity and a parameter dependent on the external variable (Stinton & Evans, 2007). This has been used in a wide variety

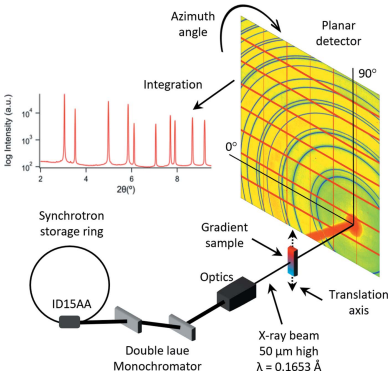

of studies to understand material structure with regards to electric field, composition, temperature, magnetic field and pressure (Daniels, 2008; Marlton *et al.*, 2017; Daniels *et al.*, 2010; Olsen *et al.*, 2017; Mabied *et al.*, 2012; Halasz *et al.*, 2010; Scarlett *et al.*, 2009). However, care must be taken when applying the parametric technique to avoid enforcing unphysical restraints on the structural model. Incorrect choice of the structural parameters' dependence on (or independence of) the external variable is the main source of error, as the resulting bias offsets the parameter uncertainties due to statistical error and fit quality. Prior knowledge of the phases involved and chemical plausibility of the model chosen are therefore essential for a correct structure parameterisation.

There are some situations where phase transitions are subtle and the structural change is small, resulting in limited peak splitting and overlapping peaks. Such transitions are difficult to parameterise and this task becomes more difficult when considering diffraction data from lower diffraction resolution two-dimensional detectors (Bernasconi & Wright, 2018; Norby, 1997). Two-dimensional detectors are key components of modern versatile diffraction setups as they allow for rapid data collection during *in situ* characterization and adjustable angular resolution to suit a variety of diffraction techniques. In this study, a technique has been developed that allows for the identification of subtle phase boundaries in a series of diffraction patterns from a compositional gradient. This method would be particularly useful for studying phase transitions *in situ* or within multi-phase complex specimens.

The technique is demonstrated in a lead-free piezoelectric material. In such materials, the search for high-performance properties has been based around the search for compositions in proximity to morphotropic phase boundaries (Rödel *et al.*, 2009; Jaffe, 1971; Shashank & Sahn, 2012; Shrout & Zhang, 2007; Takenaka *et al.*, 2008; Li *et al.*, 2013). Such compositions tend to exhibit enhanced piezoelectric properties and, hence, identification of phase boundaries in these systems is critical. We consider compositional gradients synthesized within the $(BiFeO_3)_x(Bi_{0.5}K_{0.5}TiO_3)_y(Bi_{0.5}Na_{0.5}TiO_3)_{1-x-y}(BF_xBKT_yBNT_{1-x-y})$ ternary system, which exhibits subtle phase boundaries between rhombohedral and cubic structures. This ternary system is of interest because it has been considered for many high-performance piezoelectric devices (Wefring *et al.*, 2015, 2016; Khansur *et al.*, 2016; Cheon *et al.*, 2016; Morozov *et al.*, 2012, 2014; Levin *et al.*, 2013; Bennett *et al.*, 2013; Kazushige *et al.*, 2006). Additionally, an example refinement from the $(Bi_{0.5}Na_{0.5}TiO_3)_x(BaTiO_3)_{1-x}(BNT_xBT_{1-x})$ binary system (Takenaka *et al.*, 2008) is also considered as it exhibits two phase boundaries within the compositional range tested.

2. Method

2.1. Sample preparation

End members of the $BF_xBKT_yBNT_{1-x-y}$ ternary system (BKT, BNT, $BF_{75}BNT_{25}$, $BF_{75}BKT_{25}$) were synthesized using conventional solid-state synthesis techniques using starting powders of Bi_2O_3 (99.9%), Na_2CO_3 (99.95%) (Sigma-Aldrich), TiO_2 (99.9%), Fe_2O_3 (99.998%) and K_2CO_3 (99.997%) (Alfa Aesar). The synthesis involved weighing the relevant powders in their stoichiometric ratios and then mixing in ethanol in a ball mill for 24 h. The powders were then dried, calcined at 800–900°C and re-ground in a mortar and pestle. The compositionally graded samples were prepared via a layering technique of end member powders (Marlton *et al.*, 2017). Each of these covered a compositional gradient of 12 mol% and were sintered at 1000°C. The synthesis of the BNT_xBT_{1-x} binary gradient is described by Marlton *et al.* (2017). A sample of approximately 6 mm × 0.8 mm × 0.8 mm was sectioned from the pellet with the compositional gradient along the 6 mm direction. The surfaces of the sample were then ground to a final grit size of 15 µm to ensure flat surfaces and uniform thickness along the gradient. A total of nine samples were synthesized, five of which correspond to a gradient containing 43 mol% BF and four containing 50 mol% BF. Each sample contains approximately 100–150 diffraction patterns, with a total of 709 and 542 diffraction patterns along all of the gradients containing 43 mol% and 50 mol% BF, respectively.

2.2. Synchrotron experiment

High-energy X-ray diffraction experiments were carried out at beamline ID15A of the European Synchrotron Radiation Facility. A schematic of the experiment is shown in Fig. 1. The X-ray beam was vertically focused to a height of 50 µm and monochromated to a wavelength of 0.16531 (1) Å. The sample was placed in a 1.5 mm-diameter quartz tube on the end of an alumina rod mounted on a goniometric head in the centre of a rotation stage. Diffraction images in Debye–Scherrer

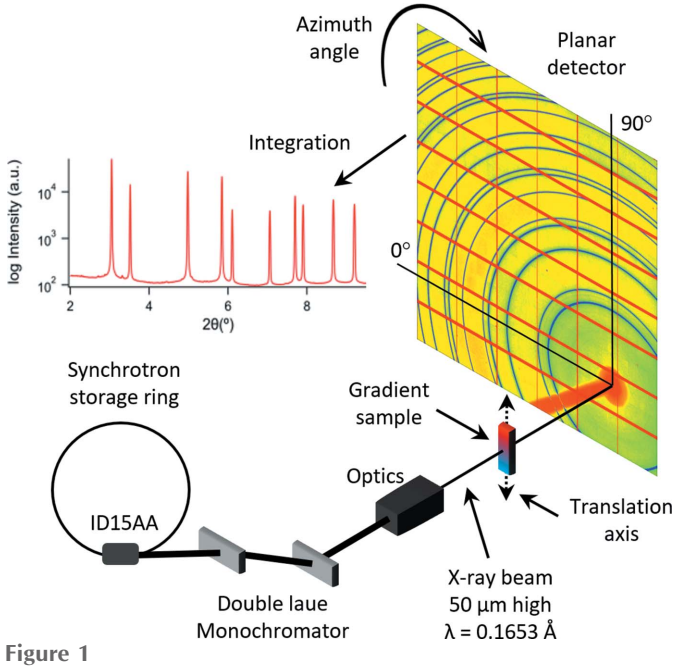

Figure 1
Schematic illustration of the high-energy synchrotron experiment. A beam with a wavelength of 0.16531 Å and a height of 50 µm penetrates the compositionally graded sample. The sample is translated vertically in 50 µm steps to scan along the compositional gradient.

geometry were recorded with a Pilatus 3X CdTe 2M photon-counting area detector positioned at 1300 mm from the sample. The sample was translated in 50 µm steps along the vertical axis and diffraction data were collected for 1 s at each position. In this geometry, the detector could collect data to a maximum 2θ of 9.5°.

2.3. Refinement process

The detector geometry was calibrated using the software *FIT2D* (Hammersley, 2016) and the two-dimensional diffraction images were converted to one-dimensional data via radial integration around the 90° of azimuth in the two-dimensional diffraction images, as shown in Fig. 1, using code written in *Igor Pro*. Masking was used to remove the pixel gaps in the detector as well as dead pixels. As the storage ring was operating in top-up mode and the flux on the sample was stable throughout the measurements, no normalization of the data was performed. The resultant diffraction patterns ranged from 2° to 9.5° in 2θ with 1500 data points.

Rietveld refinements on the resultant diffraction patterns were conducted using the software *TOPAS* (Coelho, 2008). Based on the accepted structures of the end member compositions, cubic, rhombohedral and tetragonal symmetries were refined as space groups $Pm\bar{3}m$, $R3c$ and $P4mm$, respectively (Takenaka *et al.*, 2008; Rödel *et al.*, 2009). Three different mixed-phase Rietveld refinements were conducted across the compositional gradients to assess the compositions of the phase transitions. The first refinement is referred to as the unconstrained refinement and was conducted such that there were no constraints to the lattice parameters and scale factors, which were allowed to refine freely. The second refinement is referred to as the parametric refinement and was conducted with the lattice parameters parametrically constrained. This involved determining quadratic equations to describe the lattice parameters of each phase as a function of composition,

$$a(x) = K_2x^2 + K_1x + K_0, \tag{1}$$

where x is the composition, $a(x)$ is the function for the lattice parameter with respect to composition and K_n are the polynomial coefficients. The coefficients were refined for the cubic, rhombohedral and tetragonal lattice parameters across their respective single-phase regions and then kept fixed across the whole gradient during a mixed-phase Rietveld refinement.

The third refinement is referred to as the weighted parametric refinement and was done such that the scale factor was restrained. In this case the polynomials describing the lattice parameters were kept fixed, as in the previous refinement. The scale factor was restrained using the following equation,

$$Sw_p(x) = S_p \times Fw_p(x), \tag{2}$$

where p relates to the phase, $Sw_p(x)$ is the weighted scale factor, S_p is the scale factor of an individual gradient sample and $Fw_p(x)$ is the weighting function. The weighting function is global across the compositional gradient, whereas the scale factor is refinable for each individual gradient sample. This is important as each gradient sample is slightly different in thickness and hence a single global scale factor is unsuitable. The scale factor can be slightly different for each individual composition, but it was found to be approximately constant across each individual sample.

The weighting function of choice is the inverse tan function. The inverse tan function can act as an on/off switch between the two phases and is able to have a transition period that acts as a phase boundary. This is illustrated in Fig. 2.

Fig. 2 shows the weighting functions for two different phases, labelled here as cubic and rhombohedral. The weighting functions act as a switch between 0 and 1 at the phase boundary, which is represented by the parameter b and located at the black dashed line. The c parameter can be used to tailor the width of the phase boundary, which is shown by the region highlighted in orange. The functions for each phase are exactly the same, except for the sign in front of the inverse tan function, which is positive for the phase that starts at zero to the left of the phase boundary and negative for the other. From here, the equations for the weighted scale factor for the cubic and rhombohedral phases become the following,

$$Sw_c(x) = S_c \times \frac{1}{2}\left[\left(\frac{1}{\pi/2}\right)\tan^{-1}\left(\frac{x - b_g}{c_g}\right) + 1\right], \tag{3}$$

$$Sw_r(x) = S_r \times \frac{1}{2}\left[\left(\frac{-1}{\pi/2}\right)\tan^{-1}\left(\frac{x - b_g}{c_g}\right) + 1\right], \tag{4}$$

where b_g and c_g are global refinable parameters that correspond to the position of the phase boundary and the phase boundary width, respectively. In this case, the value of c_g was fixed at 0.1. The advantage of using these weighting functions is that it forces the refinement software to find the best point along the gradient where the phase transition occurs and substantially reduces the number of refined variables.

For each of these three mixed-phase Rietveld refinements, the weight percentage of each phase could be extracted from

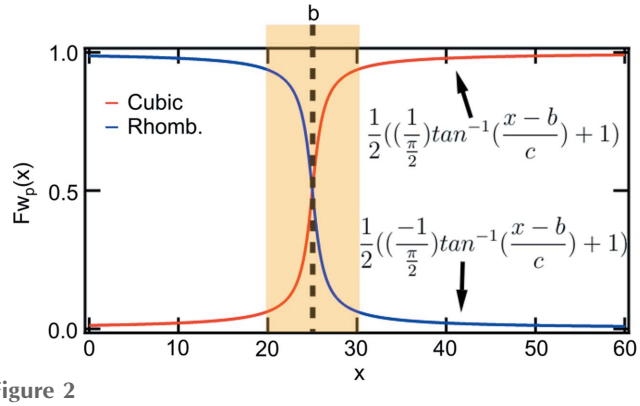

Figure 2
Scale factor weighting functions used in the weighted parametric Rietveld refinement. These inverse tan functions have been tailored such that they act as a switch between 1 and 0, with parameters that can be refined for a particular phase transition. The parameter b corresponds to the phase boundary composition, whereas c is related to the phase boundary width, where co-existence of two crystal symmetries may occur; this is indicated by the shaded orange region.

TOPAS. To ensure local minima were explored, refined parameters were slightly randomized after convergence and the refinement was repeated. This was conducted for a total of 1500 iterations, which was approximately 20 refinement (randomization) cycles. It was also assumed in each case that the composition x varied linearly along the gradient samples.

3. Results and discussion

Fig. 3(*a*) shows the samples that were produced on the $BF_xBKT_yBNT_{1-x-y}$ ternary phase diagram. Fig. 3(*b*) shows line plots for characteristic peaks from the diffraction patterns as a function of composition for gradient samples containing 43 mol% BF. These are the 113_{R3c}, 111_c and 022_c peaks. These line plots show that the peak positions along the compositional gradient overlap and there is very little observable peak splitting. The variations along the gradient are very subtle, making it difficult to discern where the phase boundary occurs. In Fig. 3(*c*), complete diffraction patterns and their fits from the weighted parametric refinement are shown for selected compositions along the gradient containing 43 mol% BF. There are small differences between the fit and the observed data. These are due to the difficulties in producing a smooth transition of the lattice parameters for the five independent compositionally graded samples. The fitting could potentially be improved through optimizing sample synthesis for smoother gradients, or additional variables and outlier exclusion rules in the parametric refinements that compensate for these errors.

Fig. 4 shows the results of the Rietveld refinement procedures on the samples with a compositional gradient containing 43 mol% BF in (*a*)–(*c*) and 50 mol% BF in (*d*)–(*f*). The weight percentage fractions of the cubic and rhombohedral phases from the refinement procedures, *i.e.* unconstrained, parametric and weighted parametric, are shown in Figs. 4(*a*) and 4(*d*), 4(*b*) and 4(*e*), and 4(*c*) and 4(*f*), respectively.

It can be seen in Fig. 4(*a*) that an unconstrained mixed-phase refinement does not provide any information as to the location of the phase boundary and also implies that the entire gradient is cubic. The parametric refinement in Fig. 4(*b*) begins to show a transition between the two different phases at approximately 25 mol% BKT. This is due to the parametric constraints guiding the fits in the correct direction. However, this is unreliable as shown by the rhombohedral end where a mixed-phase model may give the mathematical minimum in the refinement algorithm. When the weighting function is used to restrain the fit, as shown in Fig. 4(*c*), a

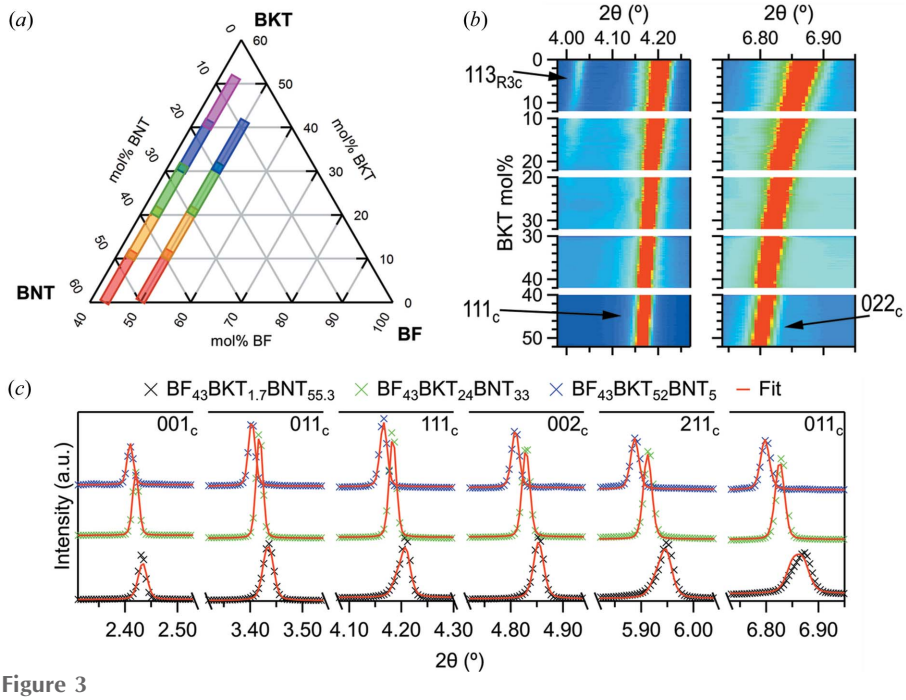

Figure 3
(*a*) Ternary phase diagram for the BF–BKT–BNT system. The coloured bars indicate the locations of each of the samples produced and measured in the current study. (*b*) Line plots for characteristic peaks along the gradient containing 43 mol% BF. The 113_{R3c} peak gradually disappears with increasing BKT content, whilst the 111_c and 022_c reflections become narrower. (*c*) Representative diffraction patterns and fits from the weighted parametric refinement for three different compositions along the gradient containing 43 mol% BF.

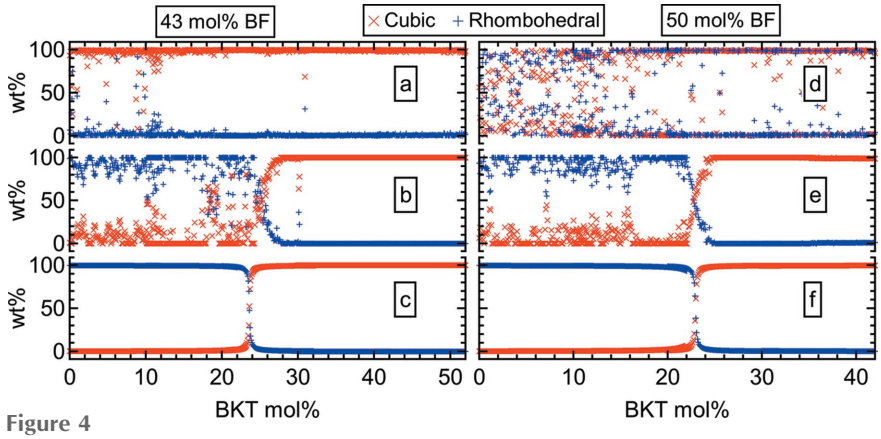

Figure 4
Phase fraction results from the mixed phase Rietveld refinements for samples containing 43 mol% (left) and 50 mol% (right) BF, with (*a*)–(*c*) and (*d*)–(*f*) corresponding to the unconstrained, parametric and weighted parametric Rietveld refinements. In (*a*) and (*d*) the refinement was conducted without constraints to the lattice parameters or scale factor and the results indicate that the entire gradient is cubic or mixed phase. In (*b*) and (*e*) the lattice parameters were constrained by a parametric refinement, which begins to show some separation between the rhombohedral and cubic regions along the gradient. However, there is a lot of noise in the rhombohedral region, which makes the boundary unclear. In (*c*) and (*f*) the restraints to the scale factor were introduced and this shows clear separation between the two phases.

clearer transition between the two phases at 23.6 mol% BKT is found.

Figs. 4(*d*)–4(*f*) shows the same fitting results for samples with a compositional gradient containing 50 mol% BF. In Fig. 4(*d*), the phase separation is worse than in Fig. 4(*a*), showing that the unconstrained mixed-phase fit does not provide any useful information. However, in Fig. 4(*e*) there is a substantial improvement to the phase separation that is also better than the results in Fig. 4(*b*). However, it still appears to be mixed phase on the rhombohedral end of the gradient. In Fig. 4(*f*), the refinement is further improved, indicating that the phase boundary occurs at 22.8 mol% BKT.

This method has also been applied to the gradient in the BNT_xBT_{1-x} system that has a gradient from BNT_{100} to $BNT_{88}BT_{12}$. This gradient shows a transition from rhombohedral to cubic to tetragonal (Marlton *et al.*, 2017). Conducting an unconstrained mixed-phase Rietveld refinement across this gradient produces the results observed in Fig. 5(*a*). Similar to the previous systems, this method produces a very unclear phase analysis. In Fig. 5(*b*), the lattice parameters have been parametrically constrained and this gives a clearer picture as to the presence of the individual phases, but still implies that much of the gradient is mixed phase. The weighted parametric Rietveld refinement produces the results observed in Fig. 5(*c*). The equations for the rhombohedral and tetragonal phases in this case are similar to those used previously. However, for the cubic phase the equation was different, being the sum of two inverse tan functions for the two different phase boundaries.

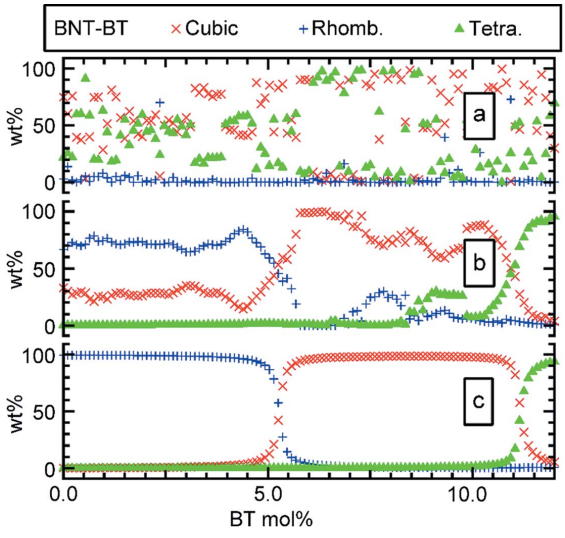

Figure 5
Phase fraction results from the mixed phase Rietveld refinements for the sample in the BNT_xBT_{1-x} system, with (*a*), (*b*) and (*c*) corresponding to the unconstrained, parametric and weighted parametric Rietveld refinements, respectively. In (*a*) the refinement was conducted with no constraints to the lattice parameters or scale factor and would indicate that the entire gradient is mixed phase. In (*b*) the lattice parameters were constrained by a parametric refinement, which begins to show some separation between the three-phase regions along the gradient. However, each region does not reach 100%, which makes the boundaries unclear. In (*c*) the restraints to the scale factor were introduced and this shows clear separation between the three phases.

This technique produces a much clearer picture of the phase transitions occurring in this system, with accurate quantification of the phase boundary compositions.

These example gradients have illustrated the difficulty in determining the location of the phase boundaries in these systems. When the mixed-phase refinement is unconstrained it is unable to discern between the different phases. When the lattice parameters become parametrically constrained, the refinement is guided in the right direction as to which peaks to fit for each phase. However, due to the close proximity of the different peaks, it falls into a mixed-phase fit even in the single-phase regions and is unable to identify where the phase boundary occurs. The addition of the weighting function restraint to the refinement drastically improves the quality of the phase analysis. This is because the weighting function guides the refinement to find the best fit across the gradient based upon the location of the phase boundary. This simplifies the fitting procedure and avoids the need to constrain other diffraction parameters such as peak width.

This technique may benefit problems where phase boundaries are difficult to discern due to low-resolution diffraction data or overlapping peaks from multiple phases with similar unit cells. In some diffraction experiments, high resolution can be attained at the cost of high-throughput *in situ* studies. The technique presented here allows for accurate identification of phase transitions from a lower-resolution high-throughput diffraction experiment. It has been demonstrated to not be limited to studying two-phase systems and can be expanded to multi-phase systems.

Acknowledgements

FM would like to acknowledge the assistance of Patrick Tung, Scarlet Kong, Lisha Liu and Lijun Wang during sample fabrication.

Funding information

This work was supported by the Australian Government under the ARC Discovery Project scheme. JD is the Director of Critus Pty Ltd. The European Synchrotron Radiation Facility is acknowledged for the provision of experiment time. FM would like to acknowledge the Australian Government Australian Postgraduate Award.

References

Bennett, J., Bell, A. J., Stevenson, T. J., Smith, R. I., Sterianou, I., Reaney, I. M. & Comyn, T. P. (2013). *Mater. Lett.* **94**, 172–175.
Bernasconi, A. & Wright, J. (2018). *Powder Diffr.* **33**, 11–20.
Cheon, C. I., Choi, J. H., Kim, J. S., Zang, J., Frömling, T., Rödel, J. & Jo, W. (2016). *J. Appl. Phys.* **119**, 154101.
Clancy, M., Styles, M. J., Bettles, C. J., Birbilis, N., Kimpton, J. A. & Webster, N. A. S. (2017). *Powder Diffr.* **32**, S54–S60.
Coelho, A. (2008). *TOPAS Academic*, version 4.1. Bruker AXS GmbH, Karlsruhe, Germany.
Daniels, J. E. (2008). *J. Appl. Cryst.* **41**, 1109–1114.
Daniels, J. E., Jo, W., Rödel, J., Honkimäki, V. & Jones, J. L. (2010). *Acta Mater.* **58**, 2103–2111.

Halasz, I., Dinnebier, R. E. & Angel, R. (2010). *J. Appl. Cryst.* **43**, 504–510.
Hammersley, A. P. (2016). *J. Appl. Cryst.* **49**, 646–652.
Jaffe, B. (1971). *Piezoelectric Ceramics.* London: Academic Press.
Kazushige, Y., Yuji, H., Hajime, N. & Tadashi, T. (2006). *Jpn. J. Appl. Phys.* **45**, 4493–4496.
Khansur, N. H., Benton, R., Dinh, T. H., Lee, J., Jones, J. L. & Daniels, J. E. (2016). *J. Appl. Phys.* **119**, 234101.
Levin, I., Reaney, I. M., Anton, E., Jo, W., Rödel, J., Pokorny, J., Schmitt, L. A., Kleebe, H., Hinterstein, M. & Jones, J. L. (2013). *Phys. Rev. B*, **87**, 024113.
Li, J.-F., Wang, K., Zhu, F., Cheng, L. & Yao, F. (2013). *J. Am. Ceram. Soc.* **96**, 3677–3696.
Mabied, A. F., Müller, M., Dinnebier, R. E., Nozawa, S., Hoshino, M., Tomita, A., Sato, T. & Adachi, S. (2012). *Acta Cryst.* B**68**, 424–430.
Marlton, F., Standard, O., Kimpton, J. A. & Daniels, J. E. (2017). *Appl. Phys. Lett.* **111**, 202903.
Morozov, M. I., Einarsrud, M. & Grande, T. (2014). *J. Appl. Phys.* **115**, 044104.
Morozov, M. I., Einarsrud, M., Grande, T. & Damjanovic, D. (2012). *Ferroelectrics*, **439**, 88–94.
Norby, P. (1997). *J. Appl. Cryst.* **30**, 21–30.
Olsen, G. H., Sørby, M. H., Selbach, S. M. & Grande, T. (2017). *Chem. Mater.* **29**, 6414–6424.
Rödel, J., Jo, W., Seifert, K. T. P., Anton, E., Granzow, T. & Damjanovic, D. (2009). *J. Am. Ceram. Soc.* **92**, 1153–1177.
Scarlett, N. V. Y., Madsen, I. C., Cranswick, L. M. D., Lwin, T., Groleau, E., Stephenson, G., Aylmore, M. & Agron-Olshina, N. (2002). *J. Appl. Cryst.* **35**, 383–400.
Scarlett, N. V. Y., Madsen, I. C., Evans, J. S. O., Coelho, A. A., McGregor, K., Rowles, M., Lanyon, M. R. & Urban, A. J. (2009). *J. Appl. Cryst.* **42**, 502–512.
Scarlett, N. V. Y., Madsen, I. C., Manias, C. & Retallack, D. (2001). *Powder Diffr.* **16**, 71–80.
Shashank, P. & Sahn. N. (2012). Editors. *Lead-Free Piezoelectrics*. New York: Springer-Verlag.
Shrout, T. R. & Zhang, S. (2007). *J. Electroceram.* **19**, 111–124.
Stinton, G. W. & Evans, J. S. O. (2007). *J. Appl. Cryst.* **40**, 87–95.
Takenaka, T., Nagata, H. & Hiruma, Y. (2008). *Jpn. J. Appl. Phys.* **47**, 3787–3801.
Wefring, E. T., Einarsrud, M. A. & Grande, T. (2015). *Phys. Chem. Chem. Phys.* **17**, 9420–9428.
Wefring, E. T., Schader, F. H., Webber, K. G., Einarsrud, M. & Grande, T. (2016). *J. Eur. Ceram. Soc.* **36**, 497–506.